Materialia 13 (2020) 100834

Contents lists available at ScienceDirect

Materialia

journal homepage: www.elsevier.com/locate/mtla

Full Length Article

Wire-arc additive manufacturing of nickel aluminum bronze/stainless steel hybrid parts – Interfacial characterization, prospects, and problems

C. Dharmendra[a,*], S. Shakerin[a], G.D. Janaki Ram[b,a,1], M. Mohammadi[a]

[a] Marine Additive Manufacturing Centre of Excellence (MAMCE), University of New Brunswick, Fredericton, NB, E3B 5A1, Canada
[b] Department of Materials Science and Metallurgical Engineering, Indian Institute of Technology Hyderabad, Kandi, 502285, India

ARTICLE INFO

Keywords:
Nickel aluminum bronze (NAB)
Stainless steel
Wire-arc additive manufacturing (WAAM)
Interface
Liquation cracking
3D characterization

ABSTRACT

Hybrid parts of nickel aluminum bronze (NAB) and 316L stainless steel were fabricated using a commercially available wire-arc additive manufacturing (WAAM) technology to evaluate the feasibility and cracking tendency. Focused Ion beam (FIB) based Scanning Electron Microscopy (SEM), Energy Dispersive Spectroscopy (EDS), Electron Backscatter Diffraction (EBSD), and Transmission Electron Microscopy (TEM) were used to characterize the built (NAB)-substrate (SS) interfacial characteristics. FIB extracted a selected region of the interface, and the spatial distribution of the interface across several sections was characterized by using the state-of-the-art technique for 3D EBSD mapping. A metallurgically bonded interface without any pores and cracks, with the inter-diffusion region in a thickness of 2 μm, was formed, which was further confirmed by a video with the results of 3D reconstructed EBSD maps. The interface did not exhibit any strong texture orientation owing to the control of the thermal gradient as NAB is more conductive than 316L. EDS elemental mapping confirmed that Fe_3Al intermetallic was formed at the NAB/SS bimetallic-joint interface. Occasional liquation cracks on the grain boundaries in the heat-affected zone (HAZ) of 316L substrate were observed. Fe-Al based intermetallic formation, along with the penetration of copper along the HAZ cracks, was noticed. The problems associated were highlighted, and remedial measures were suggested to open up the possibilities of additive manufacturing to fabricate NAB-Stainless steel hybrid parts for industrial repair and maintenance applications.

1. Introduction

Wire-arc additive manufacturing (WAAM) is emerging as a mainstream manufacturing process for the fabrication of huge metallic parts with a high volume of deposition. Compared to other direct metal additive manufacturing techniques, the main advantages of WAAM include very high deposition rates, material usage efficiency, and cost-effectiveness [1-3]. The present authors have recently reported the prospects of WAAM processing for the fabrication of nickel aluminum bronze (NAB) parts for marine applications [4].

The nickel aluminum bronze alloys (Cu-Al-Ni-Fe-Mn) are fairly microstructurally complex materials with a unique combination of properties such as low density (10% lighter than steel), high strength, high corrosion resistance, high resistance to biofouling, and excellent wear and galling resistance [5-8]. Due to these advantages, NAB end uses ranged from landing gear bearings and bushings for commercial aircraft to seawater valves and pumps, propellers for naval and commercial shipping, and non-sparking tools in the oil and gas industry [5,9,10]. Stainless steel (grades such as 304L and 316L) are widely used in the aerospace, automotive, nuclear, and offshore industries due to their high mechanical strength, corrosion, and oxidation resistance [11]. The hybrid part of NAB/316L stainless steel, composed of dissimilar alloys, presents the significant advantage of combining the heat conductivity of copper with the good mechanical property and corrosion resistance of stainless steel for industrial applications. Welding is necessary to manufacture a part that requires the joining of NAB to stainless steel (SS). However, the joining of NAB to SS using conventional welding techniques has been challenging due to the significant differences between their thermal properties, as shown in Table 1.

One of the attractive capabilities of additive manufacturing is the possibility of producing multi-material or hybrid parts for enhanced performance with cost-effectiveness measures. Such hybrid parts may be entirely produced additively using multiple metallic materials or a metallic part pre-fabricated using conventional manufacturing techniques may be used as the substrate for subsequent additive fabrication using a different metal. Manufacturing such hybrid parts using any

* Corresponding author.
E-mail address: chalasanidharmendra@gmail.com (C. Dharmendra).
[1] Dr. G.D. Janaki Ram was a Visiting Professor at the University of New Brunswick in Fredericton, New Brunswick, Canada during the completion of this work. He was formerly with the Department of Metallurgical and Materials Engineering, Indian Institute of Technology Madras, Chennai, 600036, India.

https://doi.org/10.1016/j.mtla.2020.100834
Received 3 May 2020; Accepted 15 July 2020
Available online 16 July 2020

Table 1
Thermal properties of NAB [5] and 316 L [12].

Thermal properties	NAB	SS
Melting point (°C)	1050–1075	1400 – 1450
Specific heat (J/Kg/K)	420	330
Thermal conductivity (W/m K)	42	12
Coefficient of linear expansion (20–200 °C)	17.1 × 10^{-6}/°C	16 × 10^{-6}/°C

fusion-based additive techniques needs specific considerations including: first, the dissimilar metals in question should be metallurgically compatible to avoid undesirable brittle intermetallic formation at the interface. Secondly, the dissimilar metals must not be too far apart in the galvanic series in order to avoid serious galvanic corrosion problems. Austenitic stainless steels such as AISI 316 and NAB (Cu-9Al-4Ni-4Fe-1Mn) are both popularly used in marine applications. They do not present any serious galvanic coupling problems as well [5]. Hence, NAB and 316L SS make a beneficial dissimilar metal combination for realizing marine hybrid parts.

In the literature, few works reported on laser surface modification techniques such as surface melting and cladding for the repair of cast NAB alloy components [13-18]. However, minimal work is published on arc (weld) deposition of NAB [19, 20], that too on a cast-NAB (similar composition) substrate. There is no reported work on the arc (weld) deposition of NAB on a dissimilar substrate to the authors' knowledge. Thus, the current study is taken up to establish the feasibility of producing NAB/316 L SS hybrid parts using the WAAM process. Particular emphasis is placed on understanding the microstructural characteristics at the dissimilar metal interface.

2. Experimental work

2.1. Materials and methods

Filler wires of NAB corresponding to AWS A5.7 ERCuNiAl were used in the WAAM process to deposit NAB (in 160 mm height, in 60 layers) on 10 mm thick 316L stainless steel plate in the presence of low heat input. The nominal composition (in wt.%) of the filler wire was: Cu: 79% minimum, Al: 8.5–9.5%, Ni: 4–5%, Fe: 3.5–4.5%, Mn: 0.8–1.5%. Gefertec's (based in Berlin, Germany) arc 605 WAAM equipment in gas-metal arc welding (GMAW) mode was used to deposit NAB in 60 layers. Fig. 1(a) shows the picture of deposited NAB in the form of square bars in dimensions of 160 mm height and 25 mm side. A voltage of 12.5 V with 114 Amp current, 6.5 m/min wire-feed rate, and 480 mm/min travel speed (i.e., heat input of ~170 J/mm) were used for the deposition. The settings were selected based on process parameters that produced visible defect-free parts.

2.2. Microstructural characterization

After fabricating the NAB/316L SS bimetallic component via WAAM, the bimetallic joint sample was sectioned perpendicular to the interface using a diamond-wheel cutter. The cross-section plane was wet-ground and polished using standard metallography methods followed by etching with Klemm's reagent. The interfacial microstructure was characterized using a Thermo Fisher Scientific/FEI's Scios 2 Dual-beam focused ion beam (FIB) scanning electron microscopy (SEM) fitted with an Oxford energy dispersive spectrometer (EDS). EDS analysis was used to map the elemental distribution within the interfacial region. A sample taken from the interface for electron backscattered diffraction (EBSD) analysis was mirror-polished, followed by vibratory polishing. EBSD characterization was carried out on the Scios 2 SEM system at 20 kV through an integrated Oxford/HKL EBSD detector using 0.1 μm step size. Channel 5 software was used to post-process the EBSD data. A TEM sample was extracted from the NAB-316L SS interface by using FEI Scios 2 FIB system. Thermo Scientific Themis Z TEM system operating at 200 kV was used for interfacial characterization at their facility in Hillsboro, Oregon, U.S.A.

At the same facility, EBSD tomography, which is a three-dimensional (3D) orientation microscopy, also referred to as 3D EBSD, was performed. Sequential serial sectioning by serial polishing was done using an FEI's Scios 2 FIB-SEM. An accelerated ion beam (Ga+ ions at 30 KeV) was used for automated serial sectioning via localized sputtering; and characterization of the milled 2D sections was performed by EBSD in a combined FIB-SEM. Each slice thickness was 50 nm, and the observed volume was 11 × 10 × 8.4 μm^3. The step size of about 50 nm was used for EBSD acquisition. After FIB serial sectioning acquisition, a 3D model was reconstructed from the 2D images. The angle between the ion beam and the electron beam was ~52°. As the angle between the milled surface and the imaging axis was not 90°, the raw captured images were corrected for geometrical artifacts and noise using Avizo software. Using the same software, a 3D aggregate of the EBSD microstructure was reconstructed by stacking the recorded 2D maps from all sequential slices.

An iMicroTM Nanoindentor (produced by Nanomechanics Inc.) equipped with a diamond Berkovich tip was used for the hardness measurements. The maximum load applied to the indenter was 50 mN at a constant strain rate of 0.2 s^{-1}. Line hardness measurements with 30 μm spacing were performed across the interface. An 8 × 8 array was used to map the microhardness values across the interfacial area.

3. Results

3.1. Appearance of NAB/SS component

A photograph of the WAAM-NAB deposit on 316L stainless steel substrate is shown in Fig. 1(b). A low-magnification SEM micrograph of the NAB/316L SS hybrid is shown in Fig. 1(c). As can be seen, the NAB/SS interface is flat, continuous, and sound without any fusion defects, pores, or cracks. However, the SS substrate showed some occasional cracks in the heat-affected zone (HAZ).

3.2. Microstructural features

As shown in Fig. 2, the typical microstructure of the WAAM-NAB deposit in the bulk consisted of relatively fine, equiaxed α-dendrites with globular κ_{II} and lamellar κ_{III} phase in the interdendritic regions. No interdendritic rosette-like κ_I particles were noticed in the bulk of the NAB deposit. The globular κ_{II} particles precipitate in the interdendritic regions during cooling soon after the completion of the solidification process at relatively high temperatures. The lamellar κ_{III} particles form upon further cooling at intermediate temperatures in a eutectoid decomposition reaction ($\beta \rightarrow \alpha+\kappa$). Both κ_{II} and κ_{III} are aluminide phases and contain both Fe and Ni. These microstructural features are typical of NAB after WAAM processing, where more details regarding the microstructure evolution during WAAM processing of NAB can be found from [4]. It may be noted that, the α-dendrites contain homogeneously precipitated, very fine (less than 10 nm in size) spherical-like κ_{IV} precipitates that can only be revealed in high-resolution TEM examination, as reported earlier [4]. These κ_{IV} precipitates form within the α-matrix at still lower temperatures during cooling from high temperatures. It is noted that, the κ_{IV} precipitates are too fine to be seen in the SEM micrograph presented in Fig. 2.

While the NAB deposit in the bulk (i.e., away from the SS interface) showed no rosette-like κ_I precipitates, several rosette-like κ_I particles were observed in the interdendritic regions close to the NAB/SS interface (within the first layer of the NAB deposit, shown in Fig. 3). Each layer thickness was about 2 mm during the deposition. The presence of κ_I particles was limited to a thickness of 70 μm away from the interface.

Further, a thin layer of different etch contrast, approximately 2 μm in thickness, was noticed all along with the NAB/SS interface, as shown in Fig. 4(a). This layer, presumably an intermetallic, can be seen more clearly in Fig. 4(b). EDS elemental mapping studies confirmed that this

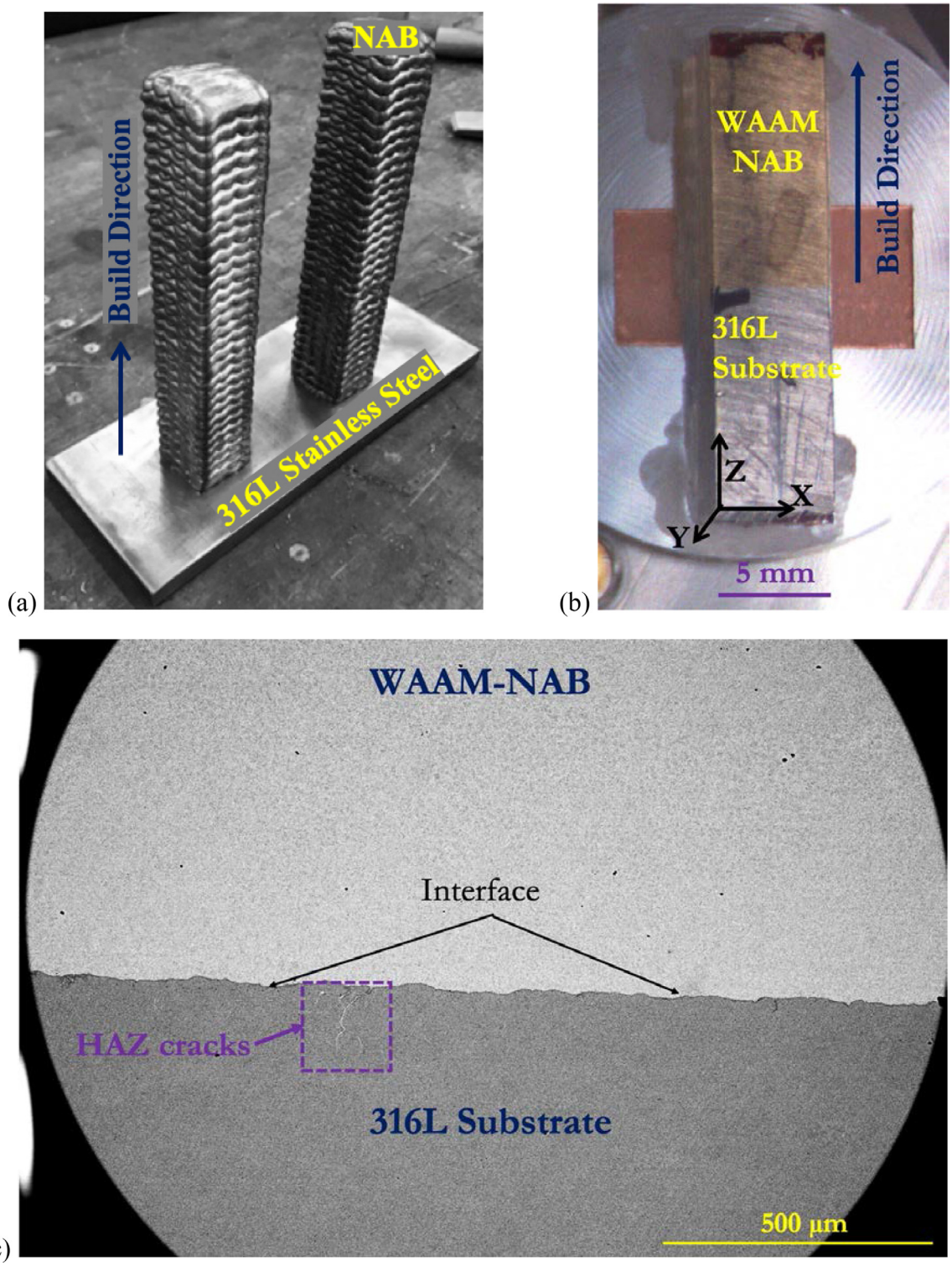

Fig. 1. (a) Picture of NAB/316L SS hybrid part, (b) photograph of WAAM-NAB deposit on 316L SS substrate, and (c) low-magnification SEM image of NAB/316L sample showing a well-bonded interface. Note occasional heat affected zone cracks in 316L substrate (boxed region).

layer is indeed an intermetallic consisting mainly of Fe and Al, as can be seen from Fig. 5. Cu, Al, Ni, Fe, and Mn were considered as alloying elements of NAB, whereas Fe, Ni, Cr, Mo, and Mn were considered for 316L SS. Further, EDS line-scan results (shown in Fig. 6(b) for the SEM image in Fig. 6(a)) of the intermetallic layer revealed much higher amount of Fe than Al suggesting that the intermetallic phase is likely to be Fe_3Al, as per the stoichiometric ratios. A line-scan analysis is used to compare the elemental distribution along the interface.

EBSD scans at the NAB/SS interface also clearly revealed the presence of a thin intermetallic layer (Fig. 7(a)) and occasional HAZ cracks (Fig. 7(b)). No epitaxial growth features were evident at the NAB/SS interface. EBSD Euler maps (Fig. 7) also showed equiaxed grains in the substrate with grain size in the HAZ is about 15–20 μm. The chemical reaction between a solid SS substrate and the melt pools of NAB gets controlled by diffusion. Under the diffusion-controlled process, the thickness of the reaction layer (X) is given as $X = K\sqrt{t}$, where K is a con-

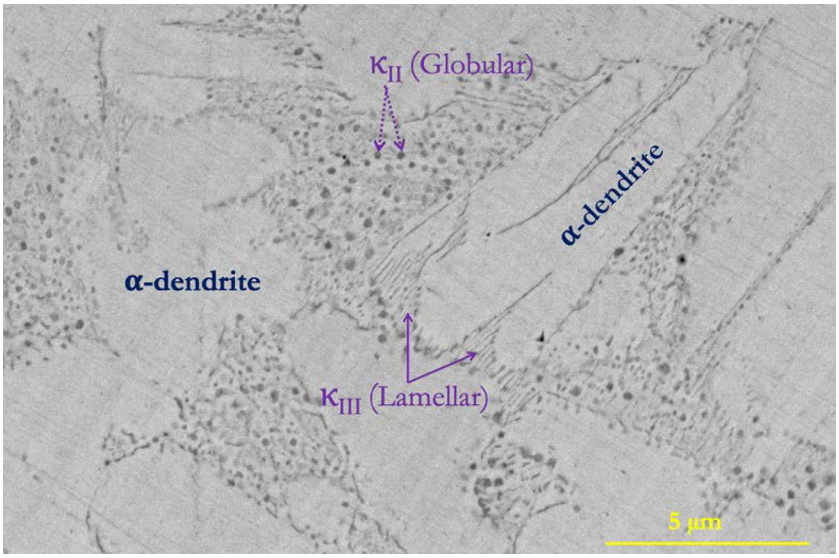

Fig. 2. SEM-BSE image of WAAM-NAB deposit in the bulk. .

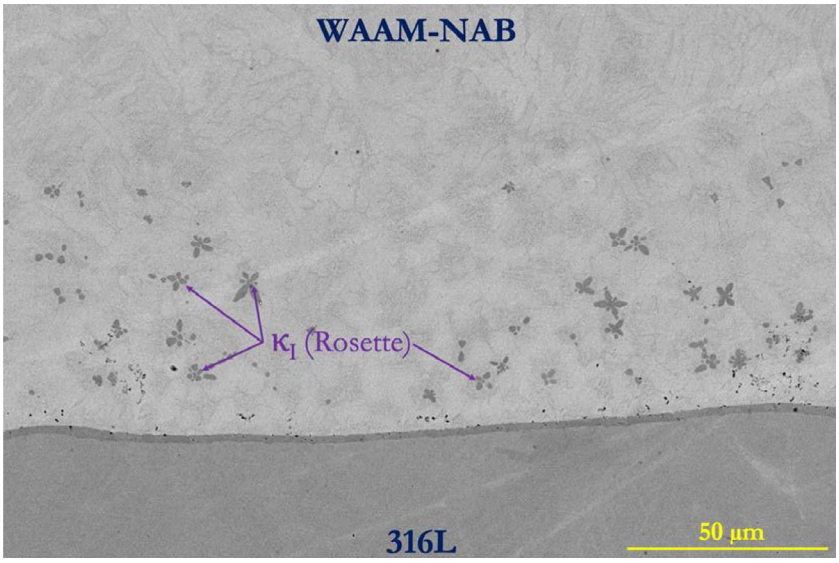

Fig. 3. SEM-BSE image from the first layer (2.5 mm thick) of the WAAM-NAB deposit revealing the formation of rosette-like κ_I in few microns (75 μm) on the SS substrate.

stant, and *t* is the time for the diffusion [21]. At high process speeds (or deposition rates) such as in WAAM, molten time was quite short; and, hence, there is no sufficient time for the growth of the interface. Thus, the interface layer formed in the WAAM-NAB/316L SS hybrid part was very thin.

Fig. 8(a) shows the boxed region in Fig. 1(b) at a higher magnification, clearly revealing the HAZ cracks in the SS substrate. The HAZ cracks were observed to form entirely along the grain boundaries of the SS substrate. Further, as can be seen from Fig. 8(b), some intermetallic formation along the HAZ cracks was noticed, which was of the same type as the intermetallic layer seen at the NAB/SS interface. Also, the HAZ cracks seemed to be filled or penetrated by liquid NAB. EDS elemental mapping of the HAZ cracks further confirmed these observations, as shown in Fig. 9. On the NAB side, at the interface, there was no diffusion of Fe into the NAB. On the other hand, Cu and Al penetrated into the cracks on austenitic grain boundaries on the SS side.

As presented in Fig. 10, TEM analysis of a selected region from the NAB-side of the interface (interfacial transition zone) was performed for further observation of the interface in view of its metallurgical bonding and inter-diffusion characteristics. FIB technique was used to extract a lamella from the interface, as shown in Fig. 10(a) and (b). After cutting the lamella, the EasyLift micro-manipulator was used to lift and rotate it for further thinning (Fig. 10(c) and (d)). Fig. 10(e) shows a high-angle annular dark-field (HAADF) image overview of the thin lamella in the scanning mode (STEM), and the difference in the contrast indicates the thickness of the intermetallic layer as ~2 μm. A high magnification image from the boxed region in Fig. 10(e) is shown in Fig. 10(f), which reveals the formation of a very thin (~20 nm) layer on the NAB side of the interface. The high-resolution TEM (HRTEM) image of the interfacial transition region on the NAB side (Fig. 10(e)), is shown in Fig. 10(g). The figure exhibits a flat interface with an interfacial grain misfit angle of about 15°. This small mismatch may indicate that the interfacial transition zone on the NAB side shows a low level of energy. EDS elemental mapping of this region (Fig. 10(e)) is shown in Fig. 11(a-e). A metallurgical diffusion interface that is rich in Ni and Al is clearly revealed on the NAB side (2 μm thick intermetallic layer is Fe-Al rich). Ni and Al diffused out from the core of the NAB to the substrate at the interfacial transition zone, i.e., interface near the NAB. The diffusion of Fe is limited to the intermetallic layer only. This may be due to the formation of Fe_3Al intermetallic that affects the further diffusion of Fe from the SS side.

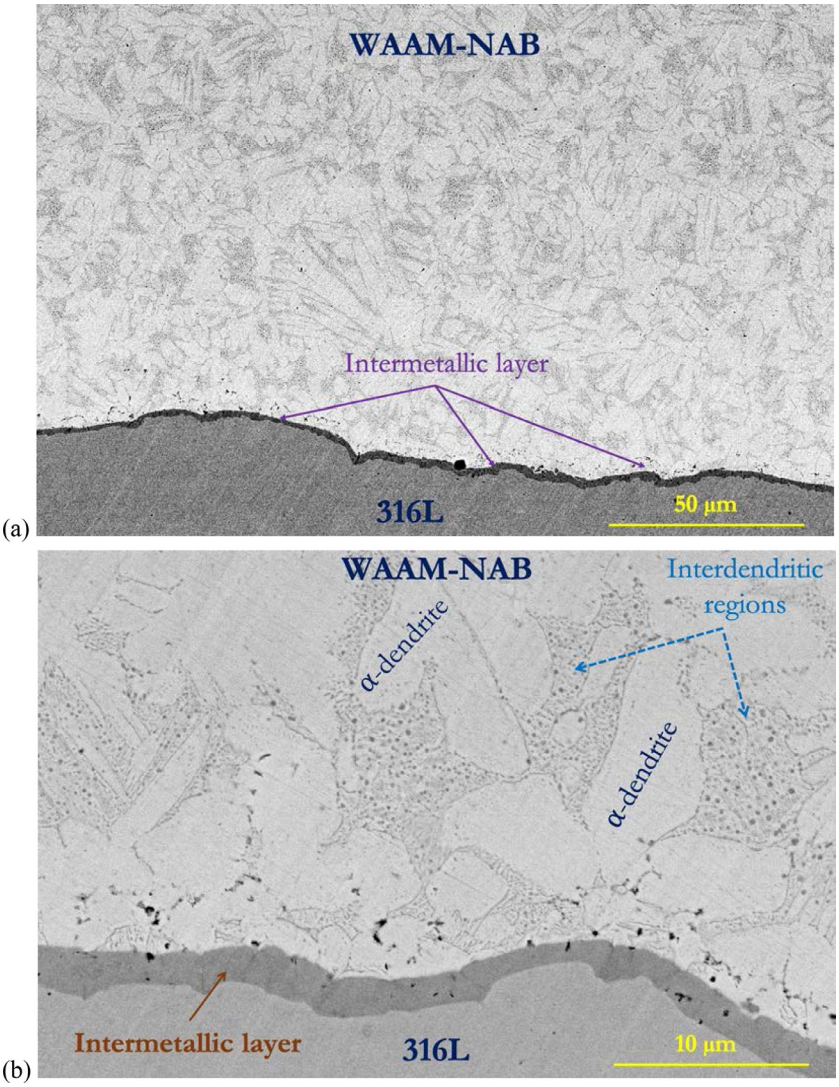

Fig. 4. SEM micrographs of the NAB/316 L sample showing a thin intermetallic layer all along with the interface.

The color-coded EBSD inverse pole figure (IPF) map of the NAB/SS interface is shown in Fig. 12(a), where <111> orientation (parallel to the surface normal) is blue, <101> is green, <001> is red, and other colors represent intermediate orientations. The texture is weak in both materials. At the NAB area, ultrafine equiaxed regions can be noticed, which are the interdendritic regions with fine κ_{II} and κ_{III} precipitates. At the interface (Fe-Al intermetallic layer), fine equiaxed grains are obtained. Fig. 12(b) presents a sequence of some 2D EBSD maps that are used for 3D grain reconstruction and a 3D orientation map revealing the interface is shown in Fig. 12(c). The color code represents IPF of the hybrid part Z-direction (build direction), where the colors are according to the inverse pole figure color triangle (in combination with the quality of volume pixel or voxel). Video 1 presents the results of 3D reconstructed EBSD maps, which shows the interface between NAB and 316L SS. The representing area is 11 μm x 10 μm x 8.4 μm and from 168 slices. Visibly sound joint without cracks is explicitly visible in this video. Supplementary material associated with this article can be found, in the online version, at doi:10.1016/j.mtla.2020.100834.

3.3. Small-scale properties

The micromechanical properties of NAB, interface layer (Fe-Al intermetallic), and 316L SS were assessed via nano-indentation measurements. Fig. 13(a) presents the indentation grid on the optical micrograph that comprises of 64 points, where the spacing between each point is ~30 μm. Fig. 13(b) presents the microhardness variations based on the color intensities. The dark blue area represents the deposited NAB, which is softer than the SS substrate that is in yellow and red colors. The change in the hardness from the NAB side was a gradual increase in the interface, followed by high hardness in the SS substrate. In the NAB, the hardness varied between 260 HV and 280 HV, whereas the hardness in the substrate varied between 320 HV and 360 HV. On the NAB side, slightly higher hardness (green color areas) correspond to κ_I (Fe_3Al, rosette-shaped) phases. Nano-hardness distribution along the interface layer is even with the constant hardness value of about 300 HV. The peak hardness was achieved around the HAZ area, the trend changed at the interface and then remained constant in the NAB side as a function of distance away from the interface. The gradual decrease in the hardness from the SS side towards the interface is due to the result of dilution of alloying elements as Cu and Al melts during deposition. In addition, the proportion of Fe decreases at the top most region of the SS side towards the interface. The typical hardness values of various Fe-Al phases are reported in literature as: FeAl: 470 HV, Fe_3Al: 350 HV, $FeAl_3$: 892 HV, Fe_2Al_5: 1013 HV, $FeAl_2$: 1060 HV [22]. The measured hardness of the NAB/SS interface was comparable to that of Fe_3Al, which is softer and confirms the observations of EDS analysis. The formation of Fe_x-Al_y intermetallic phases due to interdiffusion and reaction between Fe and

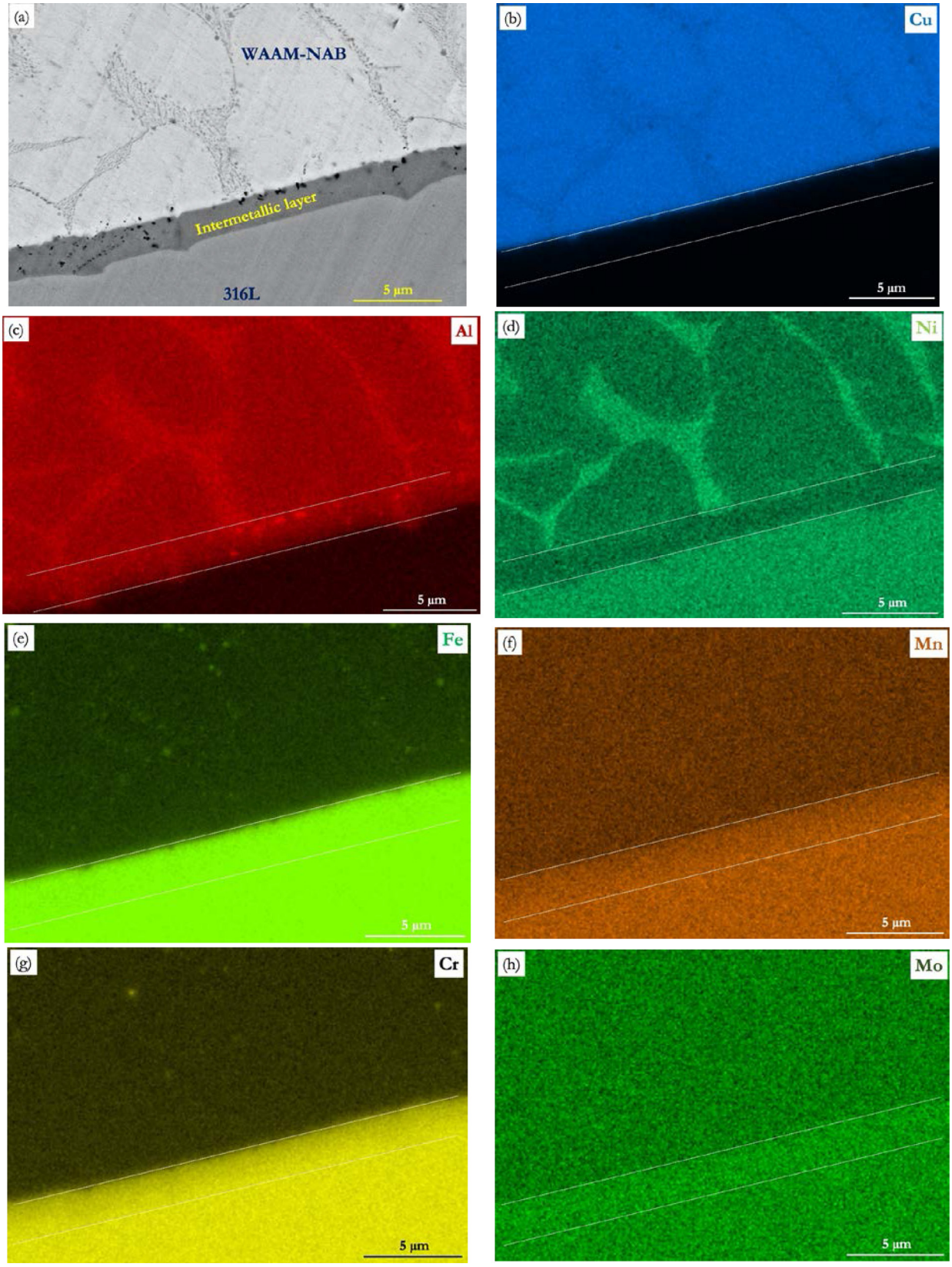

Fig. 5. (a) SEM-BSE micrograph of NAB/316L interface, and (b-f) corresponding EDS elemental maps. Note the absence of Ni and the presence of Fe and Al in the intermetallic layer.

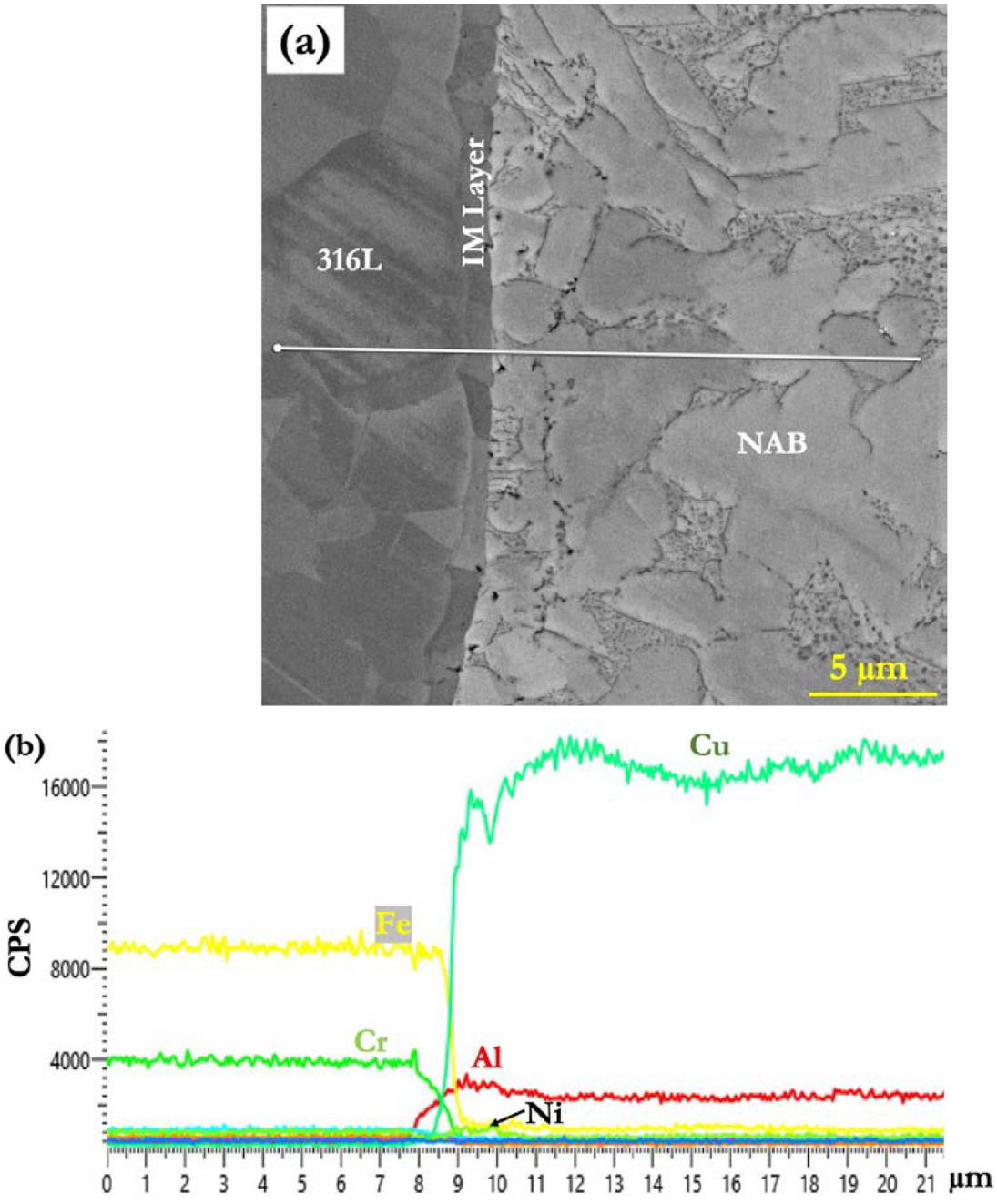

Fig. 6. (a) SEM image and (b) corresponding EDS line-scan profiles of elemental distribution across the interface of the NAB/316L hybrid-part. The values on the y-axis show the counts per second per electron-volt.

Al readily occurs in fusion welding processes [23, 24]. In the present work, the WAAM process melts the NAB wire fully, but not the SS substrate; however, partial melting of SS occurs at the interface. Therefore, the diffusion of Al from the melt pool into the SS substrate would be dominant, and the phases that can be formed are Fe-rich rather than Al-rich phases.

As shown in Fig. 13(c), the displacement (indentation depth) of the intermetallic layer is lower than the SS substrate and NAB. This probably indicates that the resistance of the intermetallic layer for plastic deformation is higher than that of SS as well as NAB. Fig. 13(d) shows that the modulus of NAB, intermetallic layer, and SS were 135 MPa, 160 MPa, and 190 MPa, respectively. The result of hardness measurements is consistent with the modulus results. The results of the load-displacement curves and modulus indicated that the Fe_3Al based intermetallic layer is not brittle.

Overall, the current findings point to three particular interface issues that can affect the properties of NAB/316L SS hybrid parts produced by the WAAM process: (i) formation of coarse κ_1 particles in the first layer of the NAB deposit close to the NAB/SS interface, (ii) formation of a continuous Fe-Al based intermetallic layer along the NAB/SS interface, (iii) formation of cracks in the HAZ of the SS substrate. The second and third issues are of more pressing concern.

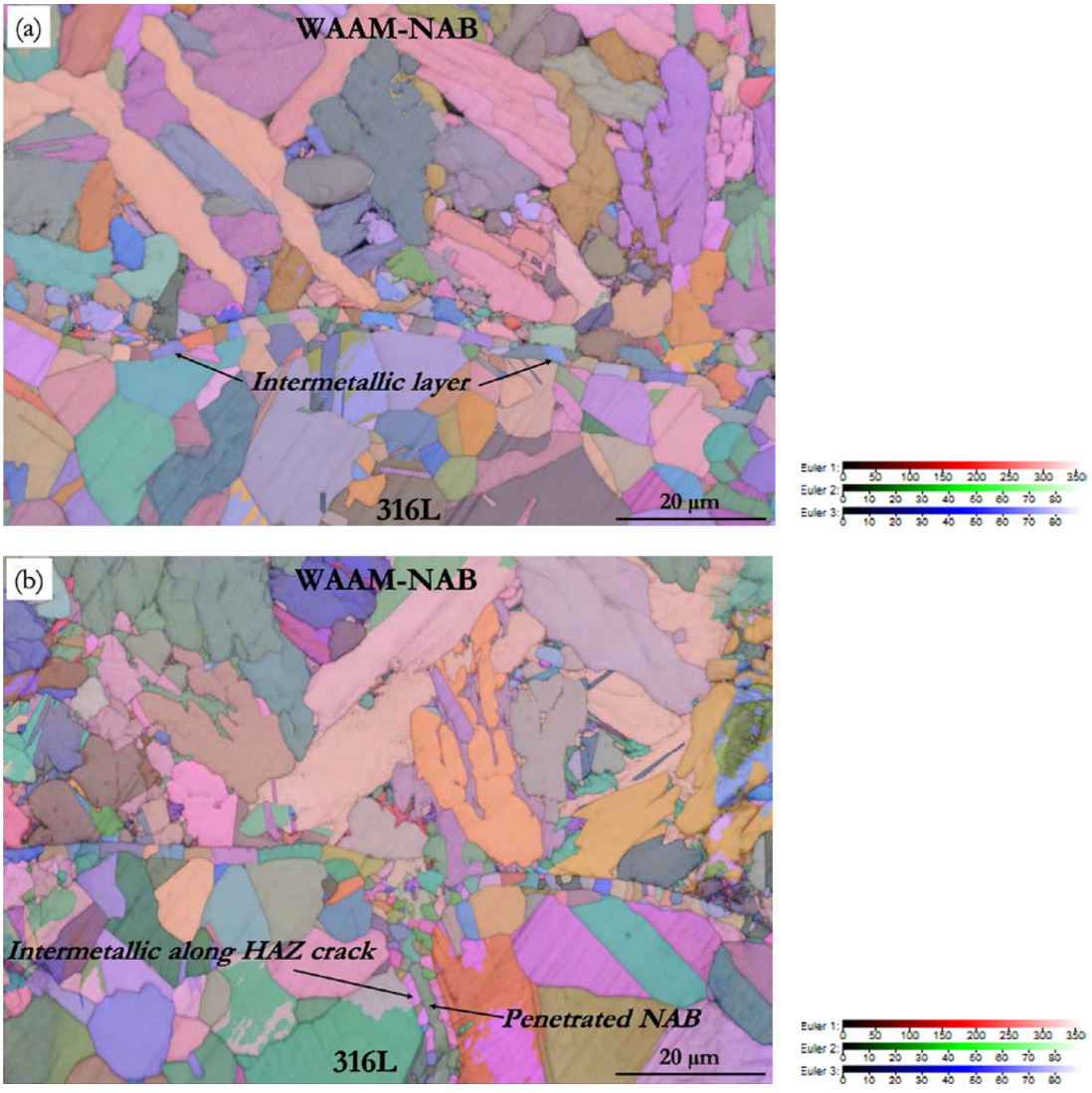

Fig. 7. EBSD Euler maps of NAB/316L SS bimetallic joint on XZ plane, which shows (a) formation of a thin and continuous intermetallic layer at the interface and (b) cracking in the heat-affected zone.

4. Discussion

4.1. Microstructure of WAAM-NAB at the interface

Coarse, rosette-like κ_I particles are invariably seen in NAB sand castings. They form during the terminal stages of solidification of the alloy (hence, their rosette-like morphology) as a consequence of extensive micro-segregation of various alloying elements. The κ_I particles contain both Fe and Ni along with aluminum, as is the case with other κ-phases. Among the various κ-precipitates, κ_I is known to be the least beneficial for the properties of the alloy. In fact, because of their coarse size, they have a marked negative effect on the toughness and ductility of the alloy. The rosette-like κ_I particles are typically completely absent in WAAM processed NAB [4], as observed in the present study in the bulk of the NAB deposit. The reduced segregation of alloying elements owing to relatively fast cooling rates in WAAM processing is responsible for this. The appearance of rosette-like κ_I particles in the first layer of the NAB deposit close to the NAB/SS interface is therefore related to dilution effects. During weld deposition of the first layer, some melting of the SS substrate is inevitable (in fact, a little bit of substrate melting is required for ensuring satisfactory bonding). The increased Fe content in the melt pools as a consequence, despite faster cooling, encourages the formation of κ_I particles during the final stages of solidification.

4.2. Formation of an interface between NAB and 316L SS

When a layer of NAB wire is melted over SS, the top surface of the substrate also melts and mixes with copper. An important consequence of SS substrate melting and intimate contact between liquid NAB and solid SS substrate during the deposition of the first layer of NAB is the formation of Fe-Al intermetallic layer all along with the interface. The formation mechanism of the interface layer in the NAB/316L SS component can be described as follows. As shown in Fig. 5, SS is melted slightly due to the action of the arc during WAAM deposition and produced a thin interface layer. With regard to the binary phase diagrams of Cu-Fe and Cu-Cr, Fe and Cr atoms in the SS substrate are given a priority in the process of liquid NAB dissolve, compared with the trace impurity elements such as Mn. The limited solubility among Cu, Fe, and Cr is due to their close atomic size and belongs to the same period (fourth) in the periodic table. The diffusion coefficient of Fe in the Cu is one order of magnitude higher than Cu in Fe [25]. When

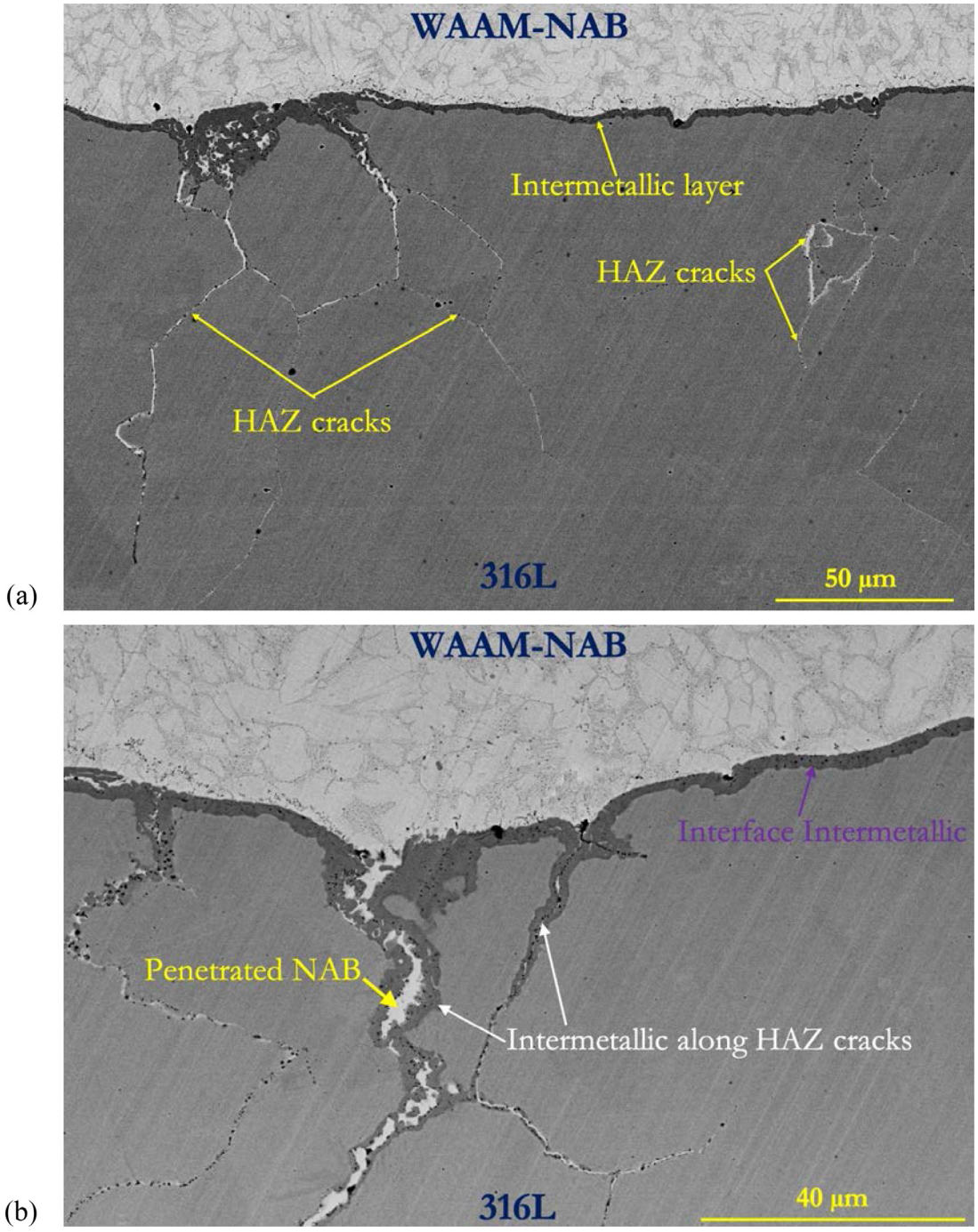

Fig. 8. (a) SEM-BSE image at WAAM-NAB/316L interface showing HAZ cracks in 316L substrate. (b) shows the penetration of NAB into and intermetallic formation along the HAZ cracks.

Fe and Cr reach their solubility limits in liquid copper in the interfacial layer, Al atoms of NAB and Fe atoms in SS can initiate reaction-diffusion.

As no interlayer is used, it naturally sets up a high chemical potential gradient across the interface for various elements. Among the constituent elements in NAB, Al can readily react with Fe (which is in abundance in the SS substrate) and form several different brittle intermetallic phases. As the chemical potential of Al is far higher in liquid Fe than that in liquid Cu [25], Al atoms diffuse strongly to liquid Fe (SS) from liquid Cu (NAB alloy) under the conditions of a chemical potential gradient. Al atoms from NAB diffused towards SS (area with high Fe-concentration) during the deposition process, which led to rich Fe-Al compounds in the interface layer. At the temperatures of WAAM deposition, which melts NAB wire completely, the process involves liquid NAB-Solid SS interaction. During this interaction, three stages may be involved: (i) wetting of solid SS by molten Cu (NAB), (ii) Dissolution of Fe (SS) into liquid Cu, and (iii) subsequent diffusion of Fe in liquid Cu. In liquid (NAB)-solid (SS) interaction, the formation of intermetallic phases/compounds is considerably faster due to the more kinetic energy of atoms in the liquid state than in the solid-state [22]. In the WAAM process, the arc melts NAB quickly, and the diffusion of Fe atoms in the molten pool of Cu accelerates. At the same time, fast deposition or the movement of the heat source controls the contact time between liquid Cu/NAB and solid Fe/SS and provides fast cooling rates. This might re-

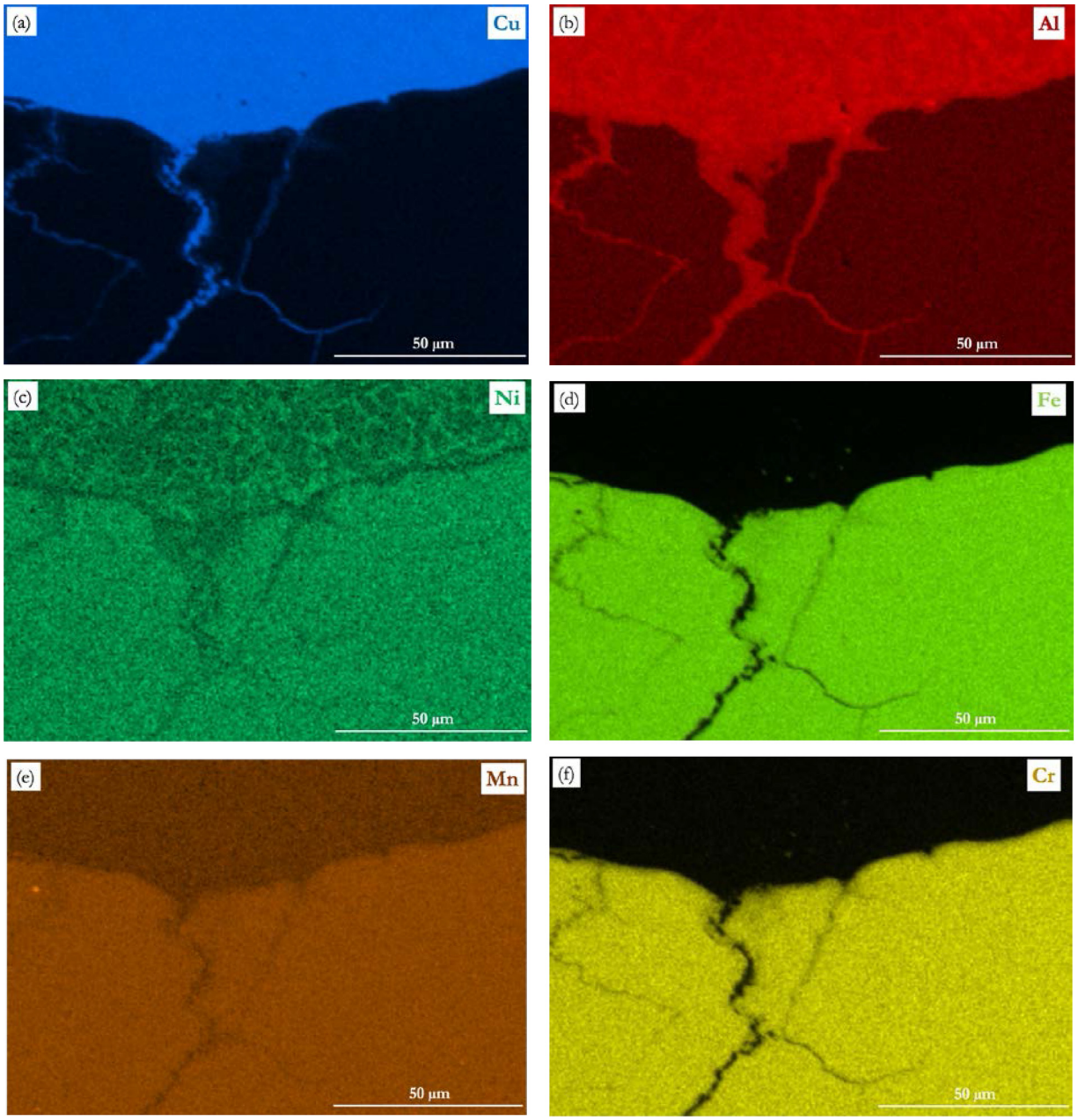

Fig. 9. EDS elemental maps corresponding to the SEM-BSE image shown in Fig. 8(b). Note the presence of Cu and Al (penetrated NAB) in HAZ cracks.

stricts diffusion to a limited depth, and hence, a thinner intermetallic layer can form.

Satisfactory metallurgical bonding at the interface of NAB/SS was also evident from the microhardness mapping. There was no abrupt change in the values of hardness while moving from the NAB to the SS substrate. The hardness values and their gradual increase are in agreement with EDS mapping results and elemental diffusion observations. The formation of the interfacial diffusion layer is due to the wetting and spread of liquid NAB on a 316L SS surface under capillary pressure gradient and the conduction of heat.

As compared to the thickness of each layer (~2 mm) deposited during WAAM, the width of the interface (in other words, intermixed region) is quite thin (2 μm). Typically, the rate of deposition in WAAM is high, and the associated travel speed plays a significant role in determining the thermal history at the interface and the thickness of the interfacial layer involving diffusion. The heat input primarily governs the thickness of the intermetallic layer at the NAB/SS interface during weld bead depositions. Excessive heat input can result in a thick intermetallic, which can easily lead to delamination at the NAB/SS interface under the influence of thermal stresses and can cause a total build failure. In the present case, the interface intermetallic layer is not too thick to result in build failure but is very likely to be thick enough to seriously affect the mechanical properties of the NAB/SS hybrid. Further work involving tensile testing of transverse specimens extracted from the NAB/316L SS hybrid can be beneficial in assessing the impact of the intermetallic layer.

As shown in Figs. 10 and 11, a layer (~20 nm) at the interfacial transition region on the NAB side is identified as NiAl based intermetallic (interdiffusion between Al and Ni) with some amount of Fe. In the NAB, concentrations of aluminum and iron were 9 and 4 wt.%, respectively. After the reaction of Al in liquid NAB with the available Fe from SS (melted region at the top) and forming Fe_3Al intermetallic layer on the SS side of the interface, remaining Al reacted with Ni and formed NiAl type thinner intermetallic layer. On the NAB side, in the vicinity of the

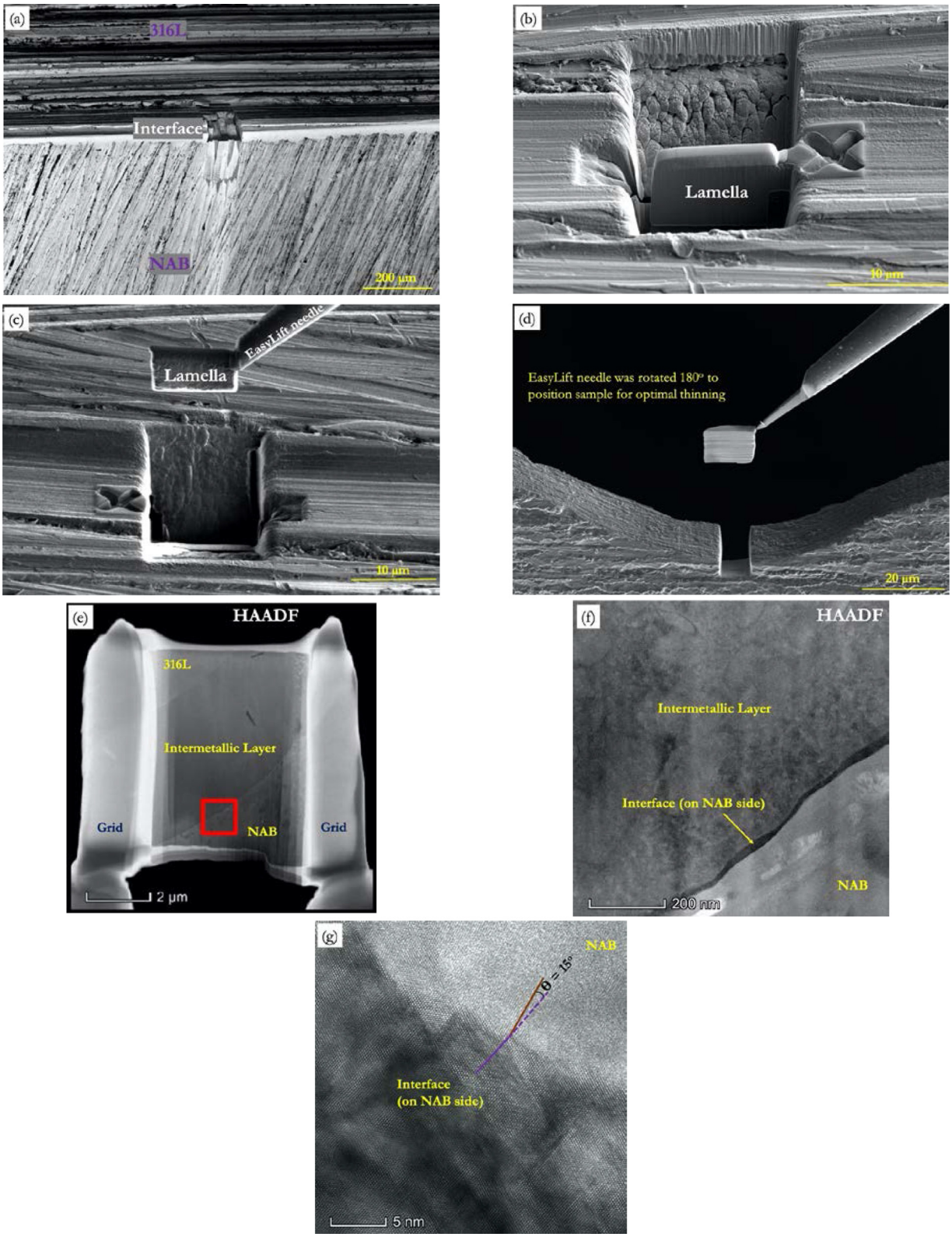

Fig. 10. (a) SEM-BSE image showing the location of a FIB extracted sample from NAB-316L SS interface, (b) Sideview of the thin lamella, (c) focused ion beam image of lamella lift out, (d) rotation of EasyLift micromanipulator, (e) STEM-HAADF imaging of interface sample on a grid, (f) STEM-HAADF image showing the interfacial morphology on NAB side, and (g) HRTEM image taken from the boxed region in (e).

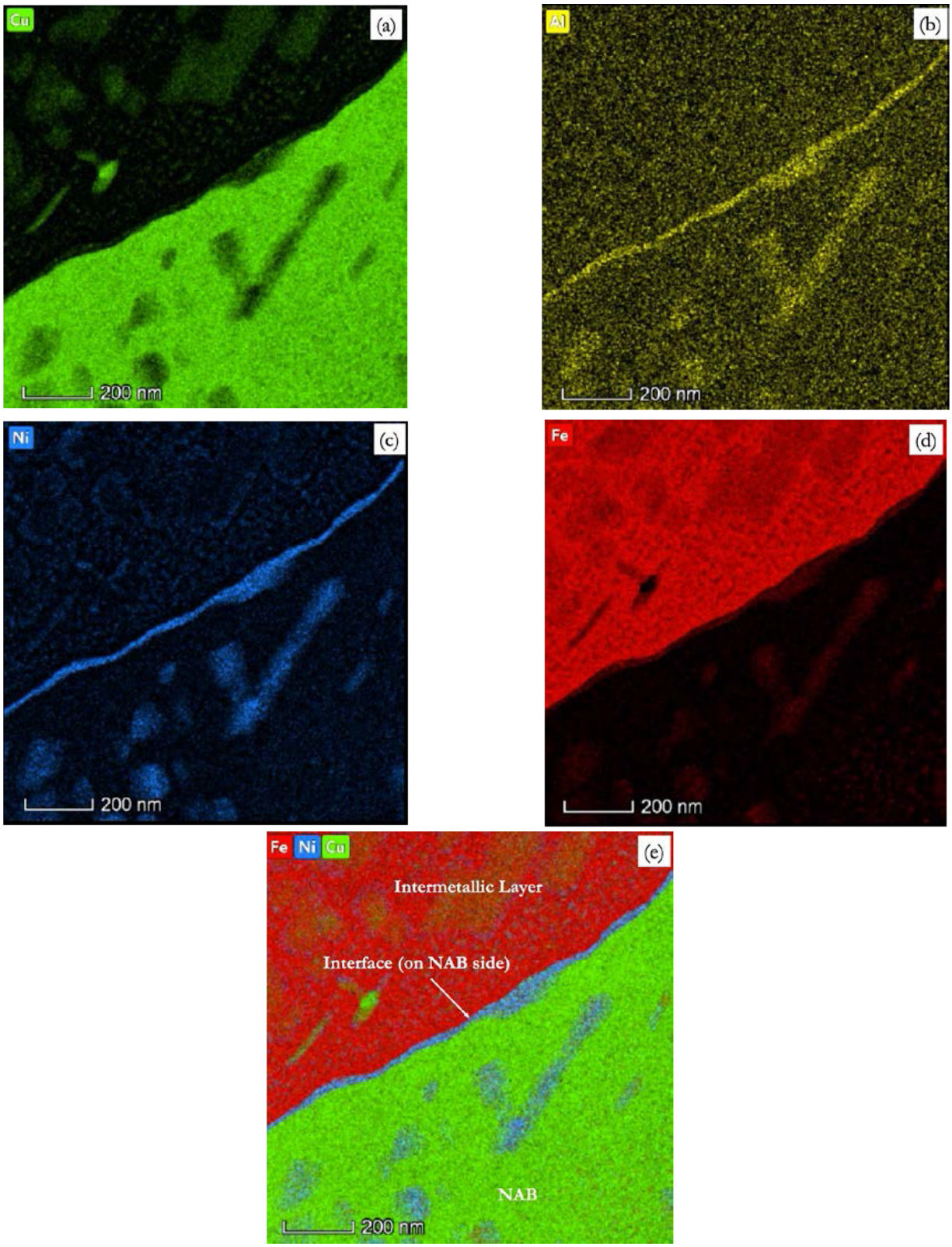

Fig. 11. EDS elemental maps from the red boxed region of the STEM-HAADF image in Fig. 11(e) for the interfacial transition zone on the NAB side. (For interpretation of the references to color in this figure legend, the reader is referred to the web version of this article.)

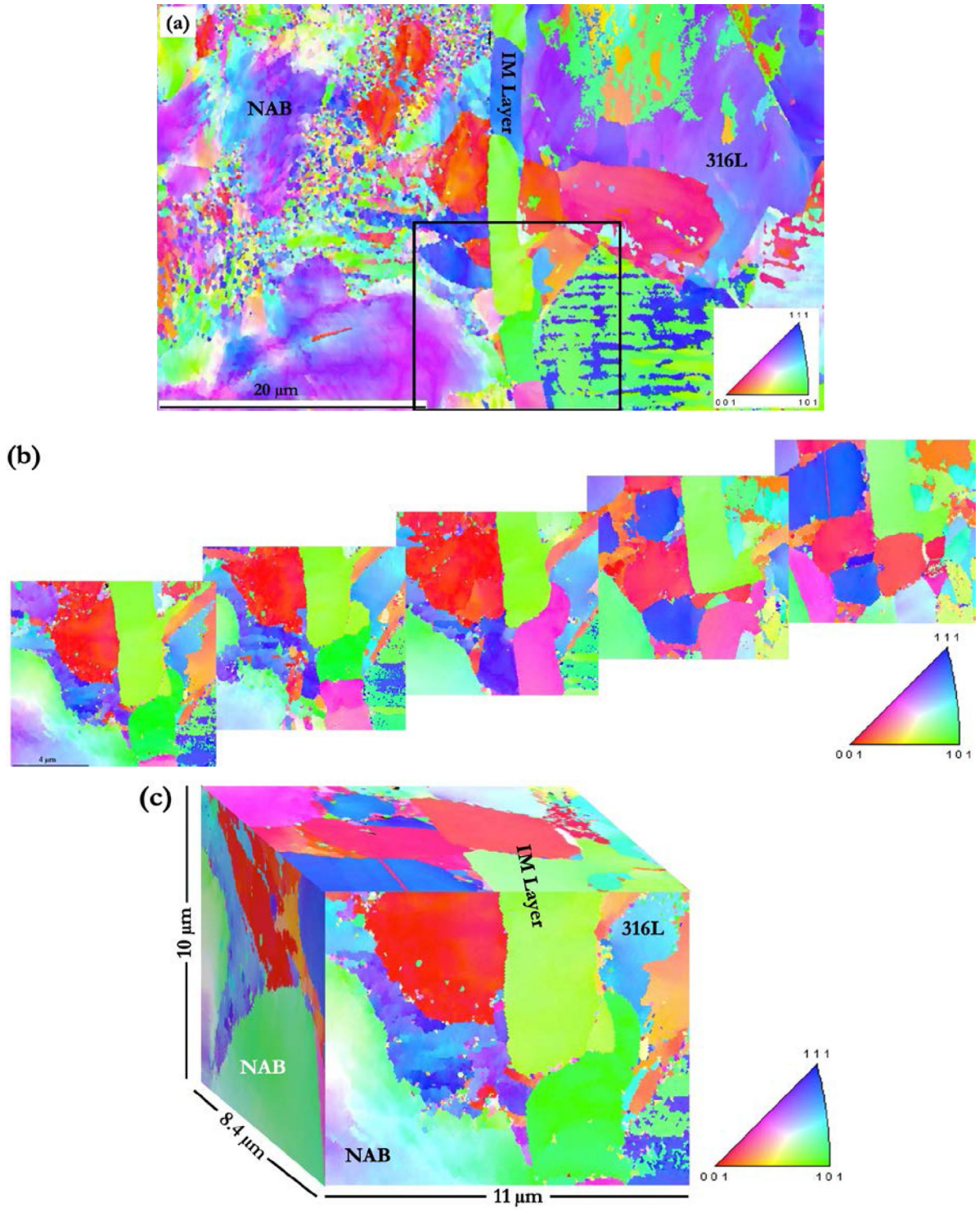

Fig. 12. (a) IPF map of NAB/316L SS part, and the black box denotes the area used for 3D acquisition, (b) sequence of few EBSD maps (2D) which are used for 3D reconstruction, and (c) 3D view revealing the interface. The color legend represents IPF of the NAB/316L hybrid part in the build direction. (For interpretation of the references to color in this figure, the reader is referred to the web version of this article.)

interfacial transition region, aluminum was dissolved from the liquid NAB.

4.3. Liquation cracking in HAZ region on 316L SS substrate

Perhaps the most significant concern in producing NAB/316L SS hybrid parts using WAAM is cracking in the HAZ of the SS substrate. Alloy 316 is known to suffer liquation cracking in the HAZ during fusion welding [26, 27]. The observation that the HAZ cracks clearly showed some penetration of NAB (Figs. 8 and 9) suggests that these cracks must have formed during the first layer of deposition. Another possibility is pure thermal stress cracking of the SS substrate. The significant difference in thermal expansion coefficient and thermal conductivity of copper (NAB) and Fe (SS substrate), can inevitably cause considerable misfit strains and residual stresses in the joint, leading to solidification cracks [27]. This is unlikely to be the cause of cracking

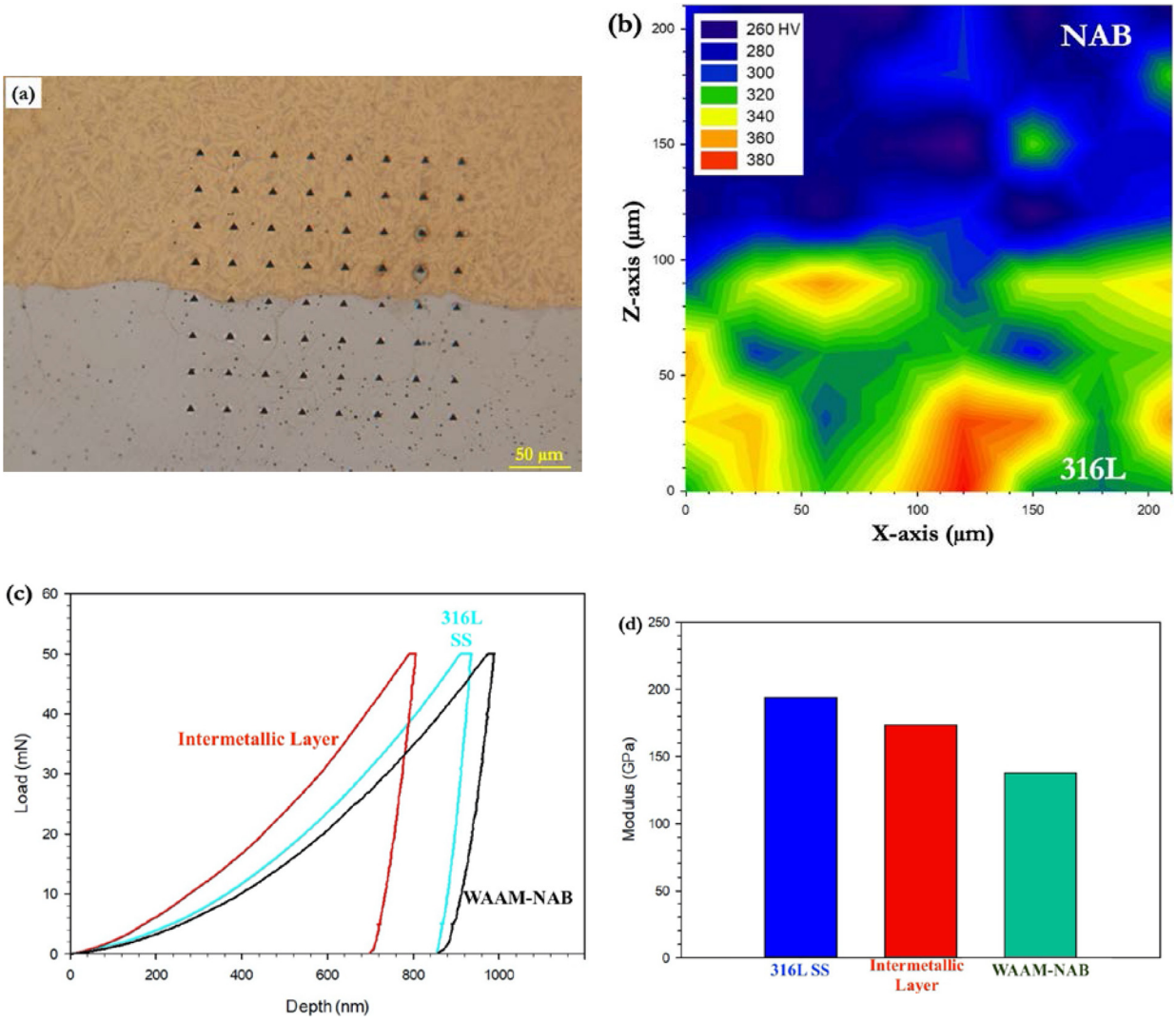

Fig. 13. Results of nanoindentation survey across NAB/316L interface: (a) optical image of the indentation grid, (b) microhardness mapping (load: 50 mN), (c) load-displacement curves, and (d) modulus of different areas. (For interpretation of the references to color in this figure, the reader is referred to the web version of this article.)

as stresses of high enough magnitude tends not to develop in the substrate during the first layer deposition. Also, such cracking does not occur entirely along the grain boundaries. Another still more remote possibility is intergranular penetration of the liquid NAB into SS substrate during the first layer deposition. Had it been the case, it should have occurred everywhere along with the NAB/SS interface – not just occasionally, as observed in the current study. Liquation cracks are intergranular, propagated in the HAZ direction, and maybe originated due to the physical property mismatch between the copper alloy and stainless steel. The presence of copper in the HAZ cracks clearly shows that the liquid copper penetrated through the HAZ grain boundaries and caused cracking during the cooling. Such behavior was also observed when 316L was welded with aluminum brass using Cu-based fillers [26].

The propensity for the formation of microcracks also depends on the available amount of copper in the melt. If there is a lesser amount, copper forms a dilute solution with iron and not significantly affect the stress-state, and thereby the probability of crack formation decreases [28]. In the present case of the WAAM process, NAB is directly deposited in a liquid state on top of the 316L SS substrate. Therefore, a higher amount of copper might lead to the formation of microcracks in the SS. Also, the capillary pressure exerted during the infiltration of copper into the austenitic grain boundaries might cause cracks to form [29, 30], which attributes to the mismatch in thermal properties and low mutual solubility.

4.4. Suggestions to obtain sound NAB/316L SS hybrid parts

Based on the current findings, it appears that producing entirely satisfactory NAB/316L SS hybrid parts through WAAM is a challenging task. It may be possible to minimize all the three problems (formation of κ_I, Fe-Al based intermetallic layer, and HAZ cracks) discussed above by further reducing the heat input during WAAM processing. However, the authors are somewhat suspicious of whether the available process window would be wide enough for accomplishing the same during industrial practice. This is particularly true concerning the problem of interface intermetallic. In any case, the following solution strategies may be considered in future work. A low-heat-input process such as laser powder deposition (cladding) may be advantageously utilized for depositing NAB on SS substrate, just to a thickness of about 1 mm or so; therefore, subsequent WAAM deposition of NAB can be expected to proceed more like depositing NAB on NAB. Another possible solution would be weld depositing a sufficiently thick layer of Cu-30% Nickel alloy on the SS substrate – during subsequent WAAM deposition of NAB, no intermetallic problem arises since the SS substrate is not in any direct contact.

Since alloy Cu-30Ni has no elements that can readily react and form intermetallics with the SS substrate, the interface intermetallic problem can be completely avoided. However, because alloy Cu-30Ni is not as strong as NAB [31], this strategy may involve some compromise on the mechanical strength of NAB/316L SS hybrid parts. Alternatively, a suitable nickel-based alloy (such as Inconel 625) may be used as the buffer layer, which can help achieve fully satisfactory mechanical strength in NAB/316L SS hybrid parts. Inconel 625 is metallurgically compatible with both Fe and Cu, as it can form a single-phase solution with both metals. However, due to the high aluminum content in the NAB, there may be a possibility of undesirable nickel-aluminide intermetallic formation at the interface. However, the problem is unlikely to be as severe as in the present case where Fe-Al based intermetallic layer tends to fail even at relatively low thermal stresses.

Regarding the HAZ liquation cracking in the substrate, stainless steel 316 is known to suffer liquation cracking in weld heat-affected zones [32]. The problem is often due to the segregation of impurities such as sulfur and phosphorous. Further, in stabilized grades, such as 316Ti, cracking can occur due to the constitutional liquation of grain boundary carbide particles [33]. In order to overcome HAZ liquation cracking problems during NAB/316L SS hybrid part fabrication, the following precautions may help. First, it is crucial to ensure a fine grain size in the stainless steel substrate (fine grain base materials are known to exhibit superior resistance to HAZ liquation cracking [34]). The presence of more grain boundaries may reduce the cooling rates as grain boundaries can act as obstacles for heat transfer and increase the time for heat flow. Secondly, close control over the impurity elements must be exercised in the substrate material. Finally, it is necessary to keep the heat input as low as possible, especially during the deposition of the first layer of NAB. Laser deposition of the first layer – whether using NAB or a suitable buffer material – is particularly helpful in this regard.

5. Conclusions

The work presented in this study showed a successful bi-metallic bond between nickel aluminum bronze and 316L stainless steel using a wire-arc additive manufacturing technique. The interface has been characterized using SEM-EDS, EBSD, and TEM, which revealed a good metallurgical bonding without any cracks. The following conclusions are drawn from this study:

(1) An intermixed interface (2 μm) was formed between NAB and 316L SS without any fusion defects and cracks. Fe-Al based intermetallic compound was formed in the region due to the elemental diffusion, as confirmed from EDS analysis. However, there is a tendency for liquation cracking in the HAZ on the stainless steel side, where copper is penetrated into the grain boundaries.
(2) Coarse, rosette-like κ_1 particles were formed on the NAB side in the first deposited layer only. The microstructure of bulk NAB did not contain any κ_1.
(3) A thin sample from the interface section was extracted by FIB and analyzed with TEM. The TEM analysis of the interfacial transition zone on the NAB side revealed a zig-zag Ni-Al based layer with 20 nm thickness.
(4) 3D EBSD mapping showed that the NAB/SS interface is smooth with continuous grains and diffusion between the NAB and SS.
(5) Hardness values of the interface layer were between that of NAB and SS.
(6) WAAM process overcomes the challenges of separation of the mixed powders that are not irradiated by the energy source during the powder-bed fusion processes. To avoid liquation cracking issues on the SS side, the following strategies may be employed.
    (i) Depositing a 1 mm thick layer of NAB by laser power deposition (cladding) on 316L SS and then depositing NAB via WAAM, which can be proceeded like depositing NAB on NAB;
    (ii) Using Inconel 625 (nickel-based superalloy) as a buffer layer due to its metallurgical compatibility with both Fe (316L SS) and Cu (NAB);
    (iii) Promoting finer grain sizes in the 316L SS substrate material.
(7) Despite the potential of WAAM for NAB-SS multi-material processing shown in this study, the limitation is the heat-treatment of the hybrid part as NAB and SS may require different heat treatment procedures. Thus, post-processing becomes complicated. There is a need to develop specific heat treatment, which is customized for additively produced NAB/316L SS hybrid parts in the future.
(8) Finally, understanding of metallurgical properties and issues of NAB and 316L SS alloys can pave the way to fabricate hybrid components of NAB and 316L using wire-arc additive processes.

Data statement

The raw and processed data required to reproduce the findings of the present work cannot be shared at this time due to technical limitations. Some data is available upon request.

Author contributions

C. Dharmendra conceived the idea, designed the experiments, analyzed the results and wrote the manuscript; S. Shakerin conducted EDS characterization and nanoindentation measurements, G.D. Janaki ram contributed to analyzing the results and manuscript preparation, M. Mohammadi conceived the idea, provided the financial support, supervised, and reviewed the manuscript.

Declaration of Competing Interest

The authors declare that they have no personal and known competing financial conflicts.

Acknowledgments

The authors would like to thank Natural Sciences and Engineering Research Council of Canada (NSERC) grant number RGPIN-2016–04221, New Brunswick Innovation Foundation (NBIF) grant number RIF2017–071, Atlantic Canada Opportunities Agency (ACOA)- Atlantic Innovation Fund (AIF) project number 210414, Mitacs Accelerate Program grant number IT10669 for providing sufficient funding to execute this work. The authors acknowledge David Polcari of FEI Instrument, Nano port, USA, for his help with arranging 3D EBSD and TEM characterization.

Supplementary materials

Supplementary material associated with this article can be found, in the online version, at doi:10.1016/j.mtla.2020.100834.

References

[1] W.E. Frazier, Metal additive manufacturing: a review, J. Mater. Eng. Perform. 23 (2014) 1917–1928, doi:10.1007/s11665-014-0958-z.
[2] D. Ding, Z. Pan, D. Cuiuri, H. Li, Wire-feed additive manufacturing of metal components: technologies, developments and future interests, Int. J. Adv. Manuf. Technol. 81 (2015) 465–481, doi:10.1007/s00170-015-7077-3.
[3] M.A. Jackson, A. Van Asten, J.D. Morrow, S. Min, F.E. Pfefferkorn, A comparison of energy consumption in wire-based and powder-based additive-subtractive manufacturing, Procedia Manuf. 5 (2016) 989–1005, doi:10.1016/j.promfg.2016.08.087.
[4] C. Dharmendra, A. Hadadzadeh, B.S. Amirkhiz, G.D. Janaki Ram, M. Mohammadi, Microstructural Evolution and Mechanical Behavior of Nickel Aluminum Bronze Cu-9Al-4Fe-4Ni-1Mn Fabricated Through Wire-Arc Additive Manufacturing, 30 (2019) 100872. 10.1016/j.addma.2019.100872
[5] I. Richardson, Guide to Nickel Aluminum Bronze for Engineers, Copper Development Association Publication, Helmel Hempstead, 2016.
[6] R.J.C. Dawson, Aluminium Bronze, Eng. Mater. Des. 22 (12) (1978) 25–28.
[7] V.A. Callcut, Aluminium bronze for industrial use, Met. Mater. 5 (3) (1989) 128–132.
[8] C. Powell, H. Stillman, Corrosion Behavior of Copper Alloys Used in Marine Aquaculture, International Copper Association, Ltd., Madison, New York, 2009.

[9] E.A. Culpan, A.G. Foley, The detection of selective phase corrosion in cast nickel aluminum bronze by acoustic emission techniques, J. Mater. Sci. 17 (1982) 953–964, doi:10.1007/BF00543513.
[10] E.A. Culpan, G. Rose, Microstructural characterization of cast nickel aluminium bronze, J. Mater. Sci. 13 (1978) 1647–1657, doi:10.1007/BF00548728.
[11] , Stainless Steel 316/316L Product Data Bulletin, AK Steel Corporation, 2013 http://www.aksteel.com/pdf/markets_products/stainless/austentic/316_316L_Stainless_Steel_PDB_201512.pdf.
[12] K.C. Mills, Recommended Values of Thermophysical Properties For Selected Commercial Alloys, Woodhead Publishing, 2002.
[13] R. Cottam, T. Barry, Laser processing of nickel-aluminum bronze for improved surface corrosion properties, J. Laser Appl. 25 (2013) 032009, doi:10.2351/1.4799555.
[14] C.H. Tang, F.T. Cheng, H.C. Man, Laser surface alloying of a marine propeller bronze using aluminium powder Part 1: microstructural analysis and cavitation erosion study, Surf. Coat. Technol. 200 (2006) 2602–2609, doi:10.1016/j.surfcoat.2004.12.021.
[15] C.H. Tang, F.T. Cheng, H.C. Man, Improvement in cavitation erosion resistance of a copper-based propeller alloy by laser surface melting, Surf. Coat. Technol. 182 (2004) 300–307, doi:10.1016/j.surfcoat.2003.08.048.
[16] C.V. Hyatt, K.H. Magee, T. Betancourt, The effect of heat input on the microstructure and properties of nickel aluminium bronze laser clad with a consumable of composition Cu-9.0Al-4.6Ni-3.9Fe-1.3Mn, Metall. Mater. Trans. A 29A (1998) 1677–1690, doi:10.1007/s11661-998-00905.
[17] R.D. Klassen, C.V. Hyatt, P.R. Roberge, Passivation of laser-treated nickel aluminum bronze as measured by electrochemical impedance spectroscopy, Can. Metall. Quart. 39 (2013) 235–246, doi:10.1179/cmq.2000.39.2.235.
[18] X. Feng, X. Cui, G. Jin, W. Zheng, Z. Cai, X. Wen, B. Lu, J. Liu, Underwater laser cladding in full wet surroundings for fabrication of nickel aluminum bronze castings, Surf. Coat. Technol. 333 (2018) 104–114, doi:10.1016/j.surfcoat.2017.10.056.
[19] D. Ding, Z. Pan, S.V. Duin, H. Li, C. Shen, Fabricating superior NiAl bronze components through wire arc additive manufacturing, Mater. Basel 9 (2016) 652–663, doi:10.3390/ma9080652.
[20] C. Shen, G. Mu, X. Hua, F. Li, D. Luo, X. Ji, C. Zhang, Influences of postproduction heat treatments on the material anisotropy of nickel-aluminum bronze fabricated using wire-arc additive manufacturing process, Int. J. Adv. Manuf. Technol. 103 (2019) 3199–3209, doi:10.1007/s00170-019-03700-7.
[21] R. Borrisutthekul, T. Yachi, Y. Miyashita, Y. Mutoh, Suppression of intermetallic reaction layer formation by controlling heat flow in dissimilar joining of steel and aluminum alloy, Mater. Sci. Eng. A 467 (2007) 108–113, doi:10.1016/j.msea.2007.03.049.
[22] M.J. Rathod, M. Katsuna, Joining of aluminum alloy 5052 and low-carbon steel by laser roll welding, Weld. J. 24 (2004) 16–26.
[23] C. Dharmendra, K.P. Rao, J. Wilden, S. Reich, Study on laser welding-brazing of zinc coated steel to aluminum alloy with a zinc based filler, Mater. Sci. Eng. A 528 (2011) 1497–1503, doi:10.1016/j.msea.2010.10.050.
[24] J. Sun, Q. Yan, W. Gao, J. Huang, Investigation of laser welding on butt joints of Al/steel dissimilar materials, Mater. Des. 83 (2015) 120–128, doi:10.1016/j.matdes.2015.05.069.
[25] D.B. Butrymowicz, J.R. Mannina, M.E. Read, in: Diffusion Rate Data and Mass Transport Phenomena For Copper Systems, International Copper Research Association, Washington, 1977, p. 177.
[26] H.W. Lee, J.H. Sung, Effect of weld metal copper content on HAZ cracking in austenitic stainless steel welded with Al brass, Sci. Technol. Weld. Join. 10 (2005) 145–148, doi:10.1179/174329305x29573.
[27] T.A. Mai, A.C. Spowage, Characterization of dissimilar joints in laser welding of steel-kovar, copper-steel and copper-aluminium, Mater. Sci. Eng. A 374 (2004) 224–233, doi:10.1016/j.msea.2004.02.025.
[28] R. Chaudhari, A. Ingle, K. Kanak, Stress analysis of dissimilar metal weld between carbon steel and stainless steel formed by transition grading technique, Mater. Today 2 (2015) 1657–1664, doi:10.1016/j.matpr.2015.07.093.
[29] J.E. Lee, D.H. Bae, W.S. Chung, K.H. Kim, J.H. Lee, Y.R. Cho, Effects of annealing on the mechanical and interface properties of stainless steel/aluminum/copper clad-metal sheets, J. Mater. Process. Technol. 187 (2007) 546–549, doi:10.1016/j.jmatprotec.2006.11.121.
[30] H. Sabetghadam, A. Zarei Hanzaki, A. Araee, A. Hadian, Microstructural evaluation of 410 SS/Cu diffusion-bonded joint, J. Mater. Sci. Technol. 26 (2010) 163–169, doi:10.1016/S1005-0302(10)60027-g.
[31] X. Mao, F. Fang, F. Yang, J. Jiang, R. Tan, Effect of annealing on microstructure and properties of Cu-30Ni alloy tube, J. Mater. Proc. Technol. 209 (2009) 2145–2151, doi:10.1016/j.jmatprotec.2008.05.023.
[32] John C. Lippord, in: Welding Metallurgy and Weldability, John Wiley & Sons, Inc, 2015, pp. 119–127.
[33] K. RamReddy, E. Nandha Kumar, R. Jeyaraam, G.D. Janaki Ram, V.S. Sarma, Effect of grain boundary character distribution on weld heat-affected zone liquation cracking behavior of AISI 316Ti austenitic stainless steel, Mater. Charact. 142 (2018) 115–123, doi:10.1016/j.matchar.2018.05.020.
[34] Sindo Kou, in: Welding Metallurgy, 2nd ed., John Wiley & Sons, Inc., 2003, pp. 321–327.